The Flying Saucer Concept for Micro Aerial Vehicles: Computational Study

Miguel Malhó Lorga Gomes
miguel.lorga.gomes@tecnico.ulisboa.pt

Instituto Superior Técnico, Universidade de Lisboa, Portugal

July 2021

Abstract

This work presents a CFD study regarding a rotating disc in flight at angles of attack 0°, 5° and 10°, seeking to investigate the potential application of such geometry in MAVs. The commercial software FLUENT was used for the simulations with IDDES. The disc geometry is circular and infinitely thin, since it has no thickness. The free stream Reynolds number was fixed at 150,000, based on the disc's diameter. The $AdvR$ was varied between 0 and 8, where $AdvR$ is the ratio between disc edge speed due to rotation and flow speed. For zero incidence, rolling and pitching moments, measured for one surface of the disc, undergo a change of signals from $AdvR = 1$ to 2, and 2 to 4, respectively. Periodic behaviour was obtained for $AdvR = 2$, as was a salient separation line, which moves upstream with increasing rotation. At $\alpha = 5°$, C_L remains roughly constant until $AdvR = 2$, since a laminar separation bubble is present on the top surface and rotation magnitudes are low. Suppression of the bubble and intense low pressure regions, caused by rotation, occur at $AdvR = 4$ and 8 and both lead to an increase in lift production. The L/D diminished with rotation. Differential rotation $AdvR = (8,0)$ leads to an increase in C_L, while case (8,-8) decreases rolling moment. The results for $\alpha = 10°$ show that differential rotation (8,0) still suppresses the separation bubble and leads to an increase in lift.

Keywords: Rotating Disc; Aerodynamics; Micro Aerial Vehicle; Computational Fluid Dynamics; IDDES.

1. Introduction

The Micro Aerial Vehicles (MAVs) are a subclass of UAVs. As the name implies, MAVs are distinguished by their small size, allowing for added stealth and versatility. Precise figures vary, but MAVs do not generally exceed 1 meter in wingspan and weigh more than 0.5 kilograms. Interest in such vehicles has grown immensely, due to the wide range of complicated missions that these futuristic drones could theoretically perform: detection of radioactivity and chemical compounds, search for survivors, improved communications in both urban and military scenarios, and infiltration in confined, closely guarded areas [1, 2].

Generally, fixed-wing MAVs operate at $Re <$ 200,000 [3]. At such low Re, laminar separation bubbles are expected to make an appearance and negatively influence aerodynamic performance. Also, due to size restrictions, Low Aspect Ratio (LAR) lifting surfaces are utilized in fixed-wing MAVs. As such, a small, saucer-shaped drone, relying purely on a rotating surface for both lift and stability seems ideal for this class of vehicles, since fragile rotors are absent and rotation might be able to control or even suppress separation bubbles.

As of yet, the resulting flow structures and aerodynamic performance at such viscous Reynolds numbers around a small, spinning surface are still largely unknown. As such, this study was envisioned with three main goals in mind: test the viability of a flying, rotating disc design as a possible MAV application; better understand the complicated interaction between disc rotation and incoming flow at low angles of attack; and explore the effects that high magnitudes of disc rotation have on aerodynamic performance.

2. Physics of a Flying Disc

2.1. Description

A flying disc can be regarded as wing with low Aspect Ratio AR, producing considerable lift at low angle of attack. For a typical wing, AR can be calculated by the following formula:

$$AR = \frac{(Wing\ Span)^2}{Wing\ Area} \tag{1}$$

which, for a circular disc with radius R_d and diameter D_d, results in:

$$AR = \frac{D_d^2}{(D_d/2)^2\pi} = \frac{4}{\pi} \approx 1.273$$

There are two key parameters governing the flight of a rotating disc: the aerodynamic upwards force, also known as lift, and the spin of the disc, which has a stabilizing effect. Both are vital but it is only the inherent interplay between the two that allows the disc to stay airborne.

Lift acts mainly on the front of the disc, ahead of the center of mass, causing an acute, unstable pitching moment, leading to a radical nose-up motion. This moment is perpendicular to the direction of rotation of the disc, and, due to gyroscopic precession, a rolling moment is induced. Fundamentally, the immediate pitch instability is avoided and the disc swerves to left or to right, depending on which direction the disc is spinning. This is of course a simplification, as the moments will seldom act exactly on a defined axis. Nonetheless, they will usually act perpendicular to the direction of rotation, making the situation described above representative of the overall stability granted by disc rotation.

2.2. Nomenclature

For sign convention, the axes of the disc and respective rolling, yawing and pitching moments (R, S and P) around the body are defined in Figure 1. The variable Ω represents the angular velocity of the disc and COP, COM refer to center of pressure and center of mass, respectively. Positive rotation implies anti-clockwise motion.

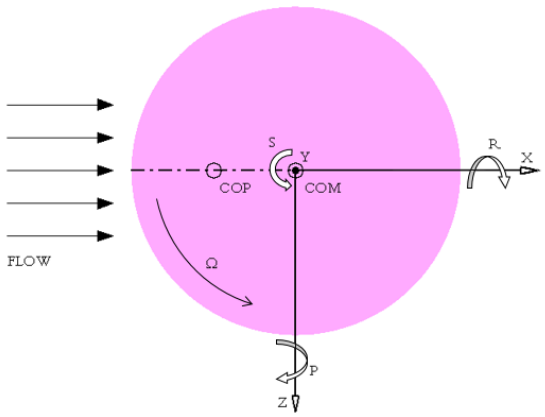

Figure 1: Orientation of the disc and sign convention.

Since the disc is rotating, it is useful to distinguish retreating and advancing side. The former refers to the side of the disc at which rotational speed and free stream velocity have the same sign and add up. This occurs at positive Z values in Figure 1. On the other hand, the latter is where these two velocities oppose each other, happening at negative Z values. The variable Advance Ratio $AdvR$ is the ratio of edge speed to flow speed. If $AdvR = 0$, the disc is not rotating, and for $AdvR = 1$, the edges of the disc are moving at the same speed as the free flow. Its formula is:

$$AdvR = \frac{\Omega R_d}{U_\infty} \tag{2}$$

where U_∞ is the free stream velocity.

Additionally, the coefficients of lift, drag and moment are calculated by:

$$C_L = \frac{F_L}{\frac{1}{2}\rho A U_\infty^2} \tag{3}$$

$$C_D = \frac{F_D}{\frac{1}{2}\rho A U_\infty^2} \tag{4}$$

$$C_M = \frac{M}{\frac{1}{2}\rho A U_\infty^2 L} \tag{5}$$

where F_L, F_D, M, ρ, A, and L are the lift force, drag force, moment, free stream density, surface area of the disc (πR_d^2) and reference length (D_d), respectively.

2.3. Literature Review

2.3.1 Experimental Studies

[4], [5] laid the foundation of aerodynamic studies of LAR wings at the typical MAV operational range (Re from 50,000 to 140,000).

[6] extensively studied the impact that different configurations of flying discs have on aerodynamic performance at Re = 378,000.

Most notably [7] tested a restrict range of Advance Ratios (between 0 and 1.04) at free stream Reynols numbers between 113,000 to 378,000. It was seen that, for pre-stall conditions, rotation has little effect on aerodynamic loads. Lift and drag curves were unchanged, but pitching and rolling moments differ only slightly for high values of $AdvR$. Some time after, the same authors remarked through smoke-wire flow visualization that the main shape of the separation bubble on top of the disc is mainly unaffected by rotation, even though it slightly shifts to the advancing side [8].

A similar study regarding the effects of disc rotation was conducted by [9]. They remarked through flow visualization of a rotating disc at Re = 110,000 and low α (0° to 5°) that the rotation helps to suppress separation at the trailing edge, by promoting transition. Also, delayed and accelerated separation is seen to occur at the retreating and advancing side, respectively.

2.3.2 Computational Studies

A purely laminar study was conducted by [10] on an ellipsoid with $AdvR$ ranging from 0 to 1.5 at Mach number 0.5 and $\alpha = 5°$. It was discovered that without rotation, a separation line appears at the top surface of the disc at roughly 70% chord. When introduced to a $AdvR$ of 1, the separation line wrapps around the left receding edge.

[11] performed LES calculations on a rotating disc in an air crossflow at Re = 13,700, in order to observe the heat transfer and changes in the wake that are brought by the spinning. With an $AdvR$ of 2, a periodic vortex shedding was reported and when the $AdvR$ was further increased to 10, a fully turbulent wake was evident. Later, the same author briefly analysed the consequent wakes of $AdvR$ = 0, 1, 2.5 and 12.5 at Re = 8,000, and remarked the evolution of the turbulent fluctuations [12].

3. The von Kármán Problem

The von Kármán swirling flow is merely composed by an infinitely long rotating planar disc immersed in still flow and, as simple as it may sound, rotation is the only factor that drives the flow. A thin boundary layer on the surface of the disc is created, due to the no-slip condition. The flow is pushed outwards, expected due to the centrifugal force, and drawn axially to satisfy mass conservation. To properly illustrate this flow problem, the typical velocity profiles are represented in Figure 2.

The rotating disc is considered in a cylindrical coordinate system as an planar infinite surface.

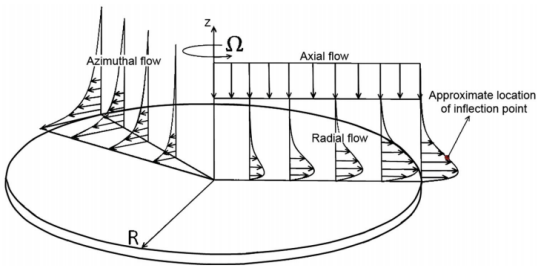

Figure 2: Visual representation of the velocity profiles from the rotating disc configuration from [13].

To handle this problem on laminar regime, von Kármán introduced a characteristic length and the following assumptions for the various velocities and pressure:

$$\xi = x \left(\frac{\Omega}{\nu}\right)^{\frac{1}{2}} \tag{6}$$

$$\begin{aligned} U_r &= \Omega r F(\xi) \qquad U_\theta = \Omega r G(\xi) \\ U_x &= (\Omega\nu)^{\frac{1}{2}} H(\xi) \qquad p = -\rho\Omega\nu P(\xi) \end{aligned} \tag{7}$$

where ξ, ν and p are the characteristic length, the kinematic viscosity and pressure, respectively.

This exchange of variables enables the derivation of an exact similarity solution of the stationary Navier-Stokes equations, allowing the full description of the flow. With the aid of $MATLAB$, the evolution of the variables F, G, H and $P - P(0)$ with regards to ξ was obtained and plotted in Figure 3.

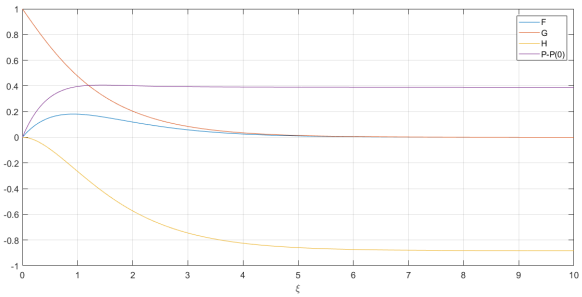

Figure 3: Evolution of F, G, H and $P - P(0)$ with ξ.

A region of low pressure is created close to the surface of the disc. Radial and tangential velocities tend to zero far from the disc and H to -0.8845.

The Reynolds number definition for rotational flows is:

$$Re_\Omega = r \left(\frac{\Omega}{\nu}\right)^{\frac{1}{2}} \tag{8}$$

[14] remarked that at Re_Ω = 510, an absolute instability was found to take place, which could potentially trigger the onset of transition to turbulent flow. Furthermore, [15] discovered that for $Re_\Omega >$ 430, a broad peak centered around $2\pi f/\Omega = 30$ appears, which is linked with the formation of stationary vortices on the disc.

The Re_Ω at the edges of the disc, or Re_{edge}, is given by:

$$Re_{edge} = R_d \left(\frac{\Omega}{\nu}\right)^{\frac{1}{2}} \tag{9}$$

3.1. Numerical Model

By simulating the von Kármán problem through CFD and further validating the results, trust is gained in the mesh, methods and models employed and confirmation that these are adequate for main problem is attained.

3.1.1 Mesh

The computational meshes used for the present and future cases were all produced through the software $ANSYS$ Meshing.

The mesh comprises a cylindrical domain. In its basis, a separate circular region was defined, to serve as the rotating disc with $R_d = 0.1\ m$, and at its center, the origin of the Cartesian coordinate system (X,Y,Z) was defined. The mesh is represented in Figure 4.

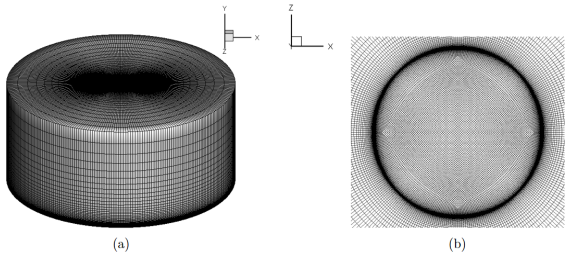

Figure 4: (a) Cylindrical mesh and (b) disc region.

Far-field boundaries were set at a distance of roughly 6 D_d from the disc, in both vertical and horizontal directions. The uppermost boundary of the domain was selected as a pressure inlet and the sides of the domain as pressure outlets. The bottom of the cylinder was considered as a symmetry plane and the rotating disc itself as a rotating wall. No slip-conditions were applied along the disc wall, meaning zero velocity and impermeability.

Two inflation layers were generated to properly capture phenomenons close to the disc. The first was in the axial direction and was constructed around the boundary layer characteristics of a rotational Reynolds close to transition, since only the laminar domain is of interest. The other refinement was created at the interface between the disc and the outer region.

The resulting mesh contained around 3.8 million nodes.

3.1.2 Discretization Schemes

The commercial package *FLUENT* was used for all simulations. This problem is steady, laminar and incompressible. Naturally, a pressure-based approach was selected as it was purposefully designed for low velocity flows. Additionally, the SIMPLE algorithm was chosen to solve the linkage between pressure and velocity. For pressure, a second-order scheme was utilized and for momentum equations, the QUICK scheme.

3.2. Problem Parameters

Three distinct cases with different Re_Ω were studied. To change this parameter, only the angular velocity of the disc Ω was altered, as the radius at which data was gathered was fixed at 30% R_d. The tested Re_Ω and the Reynolds number on the edge of the disc Re_{edge} can be seen in the Table 1.

Case	Ω [rad/s]	Re_Ω	Re_{edge}
1	0.04	1.65	5.5
2	4.38	16.50	55
3	365.18	150	500

Table 1: Values for each case.

3.3. Results

To assess the precision of the CFD results, values of G, F and H at different ξ were gathered and compared to their theoretical predictions. Figure 5 illustrates this comparison.

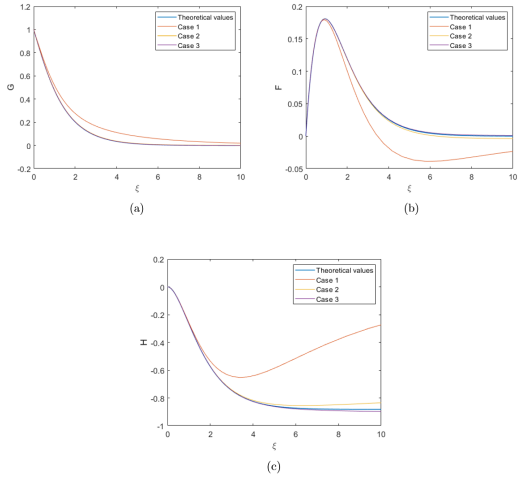

Figure 5: Evolution of (a) G, (b) F and (c) H.

Cases 2 and 3 produced excellent results, with the latter showcasing a slightly better agreement with the theoretical predictions. On the other hand, measured data from case 1 break away from the expected trend. These poor results are caused by the low Re_Ω of case 1, since the von Kármán problem considers infinite Re_Ω and thin boundary layer approximation only valid for high enough Re_Ω.

Overall, the simulations successfully replicated the von Kármán problem with the intended accuracy. The boundary conditions and used methods were deemed applicable to this kind of rotational flow.

4. Problem Formulation

As opposed to the von Kármán problem, a rotating disc will now be evaluated in flight condition at several angles of attack. As such, some new definitions are in order. The Reynolds number based on the free stream velocity is given by:

$$Re = \frac{D_d U_\infty}{\nu} \tag{10}$$

To allow comparison with previous studies, the relevant variables were adimensionalized as such:

$$\frac{p - p_\infty}{\frac{1}{2}\rho U_\infty^2} = C_p \qquad \frac{tU_\infty}{D_d} = t'$$

where t is time.

The angle of attack, or α, is defined as the inclination between the longitudinal axis of the disc and the incoming airflow. This variable was adjusted by varying the components of the incoming flow.

4.1. Numerical Model

4.1.1 Mesh

The new mesh was obtained my mirroring the one from the von Kármán problem with regards to a XZ plane. The full mesh is represented in Figure 6.

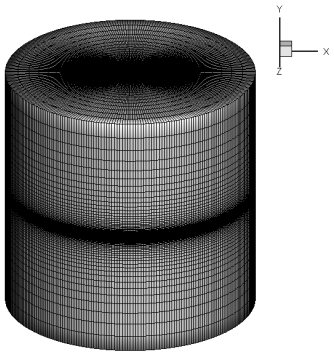

Figure 6: Final mesh.

The distance from the disc to the outer boundaries was 10 D_d. The top and bottom faces of the domain were deemed as periodic interfaces. The side face was divided in half by a YZ plane, as to consider the portion at negative X values as a velocity inlet, and the one at positive X values as a pressure outlet. At the center of domain, the disc was once again chosen as a rotating, no-slip wall.

The end result was a mesh with 7.6 million nodes.

4.1.2 Discretization Schemes

A pressure-based solver was once again chosen. SIMPLE was selected for the pressure-velocity coupling. To finalize the choice of schemes, second-order for pressure, QUICK for momentum and turbulent equations were selected once more. Implicit second-order scheme was used for time. For the time step size, $t_c = 0.005\ s$ was used.

4.1.3 Turbulence Model

For the purpose of the present numerical simulations, the model IDDES was chosen. Values of y^+ were controlled as to ensure that the viscous sublayer was always properly resolved. Turbulence intensity at boundaries was prescribed as 1%.

4.2. Problem Parameters

A Reynolds number given by the Formula 10 of 150,000 was chosen, typical for a fixed-wing MAV operation. The flow direction is (1,0,0). The disc is rotating at a fixed angular velocity Ω with both the top (+Y) and bottom surface (-Y) initially rotating in the same direction. Later, differential rotation was applied, meaning that each surface has its own $AdvR$. All tested cases are summarized on Table 2.

$AdvR$	$\Omega\ [rad/s]$	Re_{edge}
0	0	0
0.5	13.67	193
1	27.39	274
2	54.78	387
4	109.56	548
8	219.12	775

Table 2: Values for each case.

Aerodynamic coefficients of lift and drag were calculated with regards to the free stream velocity axes, and the moment coefficients relative to the body axes. The moments were taken about the center of the disc. Finally, the circular disc with $R_d = 0.2\ m$ has no thickness, to neglect gyroscopic precession. The angle of attack assumed values of 0°, 5° and 10°. For the first two, the full range of $AdvR$ was tested. However, only $AdvR = 0$ and differential rotation were simulated for $\alpha = 10°$.

5. Results for $\alpha = 0°$

5.1. Aerodynamic Coefficients

5.1.1 Full Disc

Values of aerodynamic coefficients were obtained through time averages of at least 55 t', after ensuring that a statistically steady state was reached. For the full disc, it was seen that drag and yaw increase with $AdvR$, while lift, rolling and pitching moments are zero, since the symmetric geometry of the disc at $\alpha = 0°$ produces a symmetric flow situation.

5.1.2 Half Disc

Table 3 summarizes the aerodynamic data obtained by considering only the top surface of the disc.

$AdvR$	C_L	C_D	C_M *roll*	C_M *pitch*	C_M *yaw*
0	4.62 e^{-3}	6.13 e^{-3}	0	0	0
0.5	4.98 e^{-3}	6.36 e^{-3}	-1.58 e^{-4}	1.01 e^{-3}	-1.09 e^{-3}
1	6.71 e^{-3}	6.78 e^{-3}	-1.12 e^{-4}	1.71 e^{-3}	-2.21 e^{-3}
2	1.58 e^{-2}	7.16 e^{-3}	1.14 e^{-3}	1.69 e^{-3}	-5.12 e^{-3}
4	3.73 e^{-2}	9.88 e^{-3}	4.39 e^{-4}	-3.91 e^{-3}	-1.54 e^{-2}
8	9.13 e^{-2}	1.22 e^{-2}	7.33 e^{-4}	-1.99 e^{-2}	-5.17 e^{-2}

Table 3: Mean aerodynamic coefficients for the upper surface of the disc for $\alpha = 0°$.

The increase of lift with $AdvR$ is due to low pressures near the disc, generated by rotation.

Immediately noticeable is the change of signs for both roll and pitch coefficients, occurring at the transitions from $AdvR = 1$ to 2, and 2 to 4, respectively.

5.2. Periodic Behaviour

A flow cycle was observed for $AdvR = 2$, made evident by the regular, oscillatory variation of all aerodynamic coefficients. Drag, pitching and yawing moments showcased clearer cyclic characteristics however. The frequency of this established cycle f can be expressed in adimensional form as the Strouhal Number ($S_t = fD_d/U_\infty$). The cycle takes about 10 t', or $S_t = 0.1$.

This peak in frequency spectrum occurs at much lower frequencies ($2\pi f/\Omega = 0.16$) than the one found by [15] ($2\pi f/\Omega = 30$). A periodic vortex shedding at $AdvR = 2$ for zero incidence was also reported by [11], for a disc with small thickness. However, a very different Re was used, and the reported S_t was higher than the one found in this study.

For $AdvR = 4$ and 8, this cyclic behaviour disappears.

5.3. Limiting Streamlines

Mean limiting streamlines, along with C_p contours were obtained, as in Figure 7.

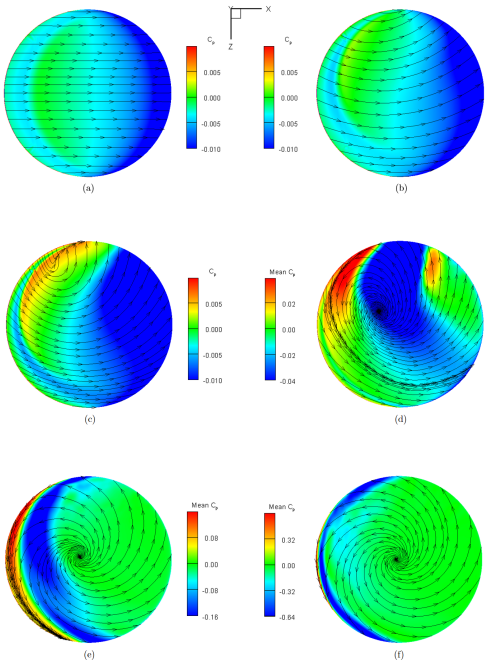

Figure 7: Mean limiting streamlines with contours of C_p for $AdvR$ = (a) 0, (b) 0.5, (c) 1, (d) 2, (e) 4 and (f) 8.

For zero rotation, the streamlines are perfectly straight. As rotation is increased to $AdvR = 0.5$, asymmetry is evident between both sides of the disc. For $AdvR = 1$, the slight adverse pressure gradient causes a small separation line, made clear by the convergence of limiting streamlines.

When $AdvR = 2$ is reached, a focus of reattachment is visible, representing the suction of the flow due to rotation. Additionally, the separation line migrated upstream, coincident with the adverse pressure gradient. The separation line effectively divides regions where rotation and convection by the outer flow dominate. [10] reported a similar separation line for $AdvR = 1$ but on the retreating side. The fact that the tested geometry had thickness and a much higher free stream velocity was utilized (Mach = 0.5) might explain this disparity.

Further increasing the magnitude of rotation to $AdvR = 4$ and 8 moves the separation line to the leading edge and approximates the topology of the streamlines to that of a pure rotation problem, as the focus migrates to the center of the disc.

Overall, after a critical $AdvR$ is reached, the effect of rotation on the periphery of the disc becomes intense enough to oppose the convective transport of the outer flow. It generates a separation line which pushes back the flow to the edges and can project fluid particles with sufficient force to leave the surface of the disc.

6. Results for $\alpha = 5°$

6.1. Aerodynamic Coefficients

Now the problem ceases to be symmetric. Therefore, only the aerodynamic data regarding the full disc is of interest. Table 4 summarizes the results.

$AdvR$	C_L	C_D	L/D	C_M *roll*	C_M *pitch*	C_M *yaw*
0	0.181	2.56 e^{-2}	7.07	0	-4.70 e^{-2}	0
0.5	0.181	2.60 e^{-2}	6.96	0	-4.71 e^{-2}	-2.14 e^{-3}
1	0.182	2.68 e^{-2}	6.79	-2.65 e^{-4}	-4.75 e^{-2}	-4.37 e^{-3}
2	0.183	2.81 e^{-2}	6.51	-1.48 e^{-3}	-4.75 e^{-2}	-1.01 e^{-2}
4	0.197	3.63 e^{-2}	5.43	-2.67 e^{-3}	-4.75 e^{-2}	-3.08 e^{-2}
8	0.241	4.54 e^{-2}	5.31	-2.56 e^{-3}	-5.20 e^{-2}	-0.104

Table 4: Mean aerodynamic coefficients for $\alpha = 5°$.

Lift stays approximately constant until $AdvR = 2$. This trend was confirmed by the findings of [7] up to $AdvR = 1.04$. However, when $AdvR = 4$ is reached, C_L increases roughly 8% and after $AdvR = 8$, a substantial increase of 22% is observed. Drag follows a similar trend than that of zero incidence, as it increases with rotation. The L/D is severely worsened at $AdvR = 4$, but at $AdvR = 8$, the massive increase in lift almost balances the increase in drag, only leading to a small decrease of lift to drag ratio. Pitching moment is roughly constant until $AdvR = 8$, at which point it increases in magnitude.

6.2. Limiting Streamlines

6.2.1 Top Surface

Figure 8 showcases the mean limiting streamlines on the top surface of the disc along with C_p contours.

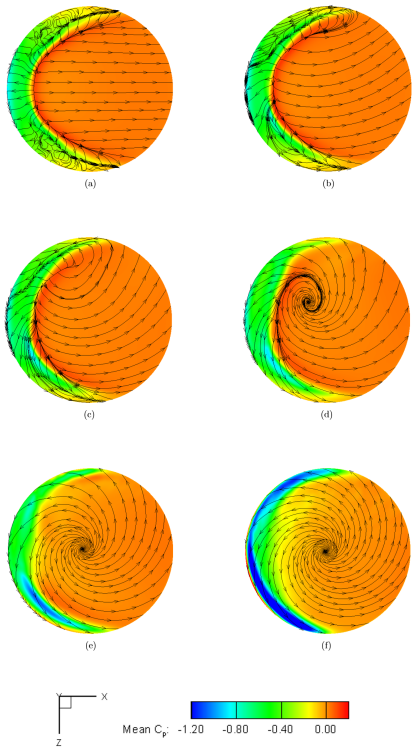

Figure 8: Mean limiting streamlines with contours of C_p for $AdvR$ = (a) 0, (b) 0.5, (c) 1, (d) 2, (e) 4 and (f) 8 for the top surface.

Starting from $AdvR = 0$, a separation and reattachment line are immediately noticeable on the front, signaling the presence of a laminar separation bubble (LSB). Here, flow reversal towards the leading edge occurs and the fluid particles are convected to the sides, where they eventually join other separation lines, representing here the tip vortices.

Adding rotation of $AdvR = 0.5$ and 1 causes a shift of the LSB, like the flow observations from [8].

For $AdvR = 2$, the separation lines on the side cease to appear, meaning that the tip vortices are not created directly on the surface, as if prevented to do so by the rotation. Also, like in Figure 7 (d), a reattachment focus is present. Here, rotation is strong enough to generate suction and expelling fluid particles in a centrifugal motion. The separation and reattachment line are still present, the latter emerging from the focus. This represents a complex separation pattern, similar to a tornado-like vortex, where fluid from the LSB is drawn to the disc due to rotation.

Finally, for high rotation values $AdvR = 4$ and 8, a pure rotation topology is obtained, as in zero incidence (Figures 7 (f)) and thus the LSB is fully suppressed.

Focusing on the contours of pressure, the distribution barely changes up until $AdvR = 2$. Pressure stays approximately constant on the center region of the LSB and increases in the vicinity of the separation lines on the sides. Only after $AdvR = 4$, when the LSB is suppressed, that strong, low pressure regions start to appear. Indeed, at $AdvR = 8$, intense negative pressure regions cover the entirety of the leading edge, strongest near the retreating side.

6.3. Bottom Surface

The same distributions for the bottom surface are represented in Figure 9.

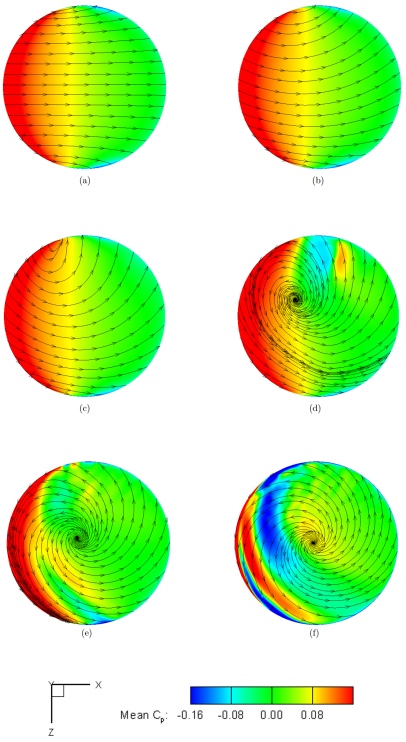

Figure 9: Mean limiting streamlines with contours of C_p for $AdvR$ = (a) 0, (b) 0.5, (c) 1, (d) 2, (e) 4 and (f) 8 for the bottom surface.

The patterns drawn by the limiting streamlines are the same as for zero incidence, in Figure 7. However, C_p contours are radically different. As expected, a high pressure region occupies the front, where the flow directly collides with the surface. As rotation takes hold, this region decreases in size and migrates to the leading edge and, for $AdvR = 8$, it shares the front with equally intense low pressure regions.

6.3.1 Discussion

From Table 4, It was seen that C_L increases for $AdvR = 4$ but the biggest improvement was from $AdvR = 4$ to 8. A reasoning behind this evolution can be accomplished by considering the results from section 6.2.1. The pressure contours are almost equal until $AdvR = 4$ and a LSB is evident. This is why C_L is practically constant between these cases. Low enough pressure is only created with high values of Ω, so low rotation magnitudes, coupled with the presence of the LSB, which forces a plateau of pressure, leads to virtually constant C_L values for low $AdvR$, up to 2. With increased rotation, the separation bubble is fully suppressed at $AdvR = 4$ and a low pressure region is seen on the retreating side. Both factors cause a mild increase in lift. However, the biggest jump comes as a consequence of the intense low pressure regions, covering most of the leading edge for $AdvR = 8$. It can be deduced that the elimination of the LSB is fundamental to achieve increase in lift for fixed incidence. This suppression not only increases lift by itself, but also allows the creation of low pressure regions on the top surface more efficiently due to rotation, further boosting C_L.

Moreover, it can be argued that the bottom surface does not play a pivotal rule in the lift evolution. At $AdvR = 4$ and 8, low pressure regions, consequence of the high degree of rotation, are created on this surface as well, albeit with much lower dominance, which undoubtedly worsen C_L. However, at these values of $AdvR$, lift is seen to increase. As such, the biggest contribution of this lower surface is the increase in drag it brings, since its effect on lift is not determinant.

The high concentration of negative pressure on the leading edge for $AdvR = 8$ is also responsible for the increase in pitching moment. This region and high pressure areas in the bottom surface lead to the most adverse C_M *pitch* of all cases, even though negative pressure is also evident on the lower surface (Figure 9 (f)), which would help counteract the one on top.

Overall, high values of rotation ($AdvR = 4$ and 8) allow for an increase in C_L, but also in C_D and C_M *pitch*, which undoubtedly worsen aerodynamic performance. However, for a real life disc with mass, the unstable pitching moment would be translated into a rolling moment by gyroscopic precession, as explained in section 2.

6.4. Differential Rotation

Better aerodynamic performance can undoubtedly be accomplished by imposing different degrees of rotation on the top and bottom surfaces of the disc. The two simulated cases with differential rotation are listed in Table 5. Here, negative $AdvR$ implies clockwise rotation. This selection of $AdvR$ was carried out with the purpose of trying to maximize L/D and reduce the unstabilizing moments. Since $AdvR = 8$ on top produced the best C_L results, only the rotation of the bottom surface was altered.

Case	Top $AdvR$	Bottom $AdvR$
1	8	0
2	8	-8

Table 5: The choice of $AdvR$ for differential rotation.

The aerodynamic data is summarized in Table 6.

Case	C_L	C_D	L/D	C_M *roll*	C_M *pitch*	C_M *yaw*
1	0.253	3.87 e^{-2}	6.54	-3.27 e^{-3}	-5.87 e^{-2}	-5.17 e^{-2}
2	0.239	4.76 e^{-2}	5.02	-5.32 e^{-4}	-5.74 e^{-2}	-7.21 e^{-4}

Table 6: Mean aerodynamic coefficients for differential rotation.

The resulting limiting streamlines and pressure contours on the top surface are the same as Figure 8 (f) for both cases. The bottom surface however, resulted in the same configuration as Figure 9 (a) for case 1, and a shifted Figure 9 (f) for case 2.

Lift increases for case 1, when compared to equal rotation of $AdvR = 8$ on both surfaces (Table 4). Now, the bottom surface is free of any rotation and thus of induced negative pressure regions. Therefore, the negative impact that these had on C_L is gone, leading to an increase in lift production. Case 2 results in approximately equal C_L to $AdvR = 8$ on both sides, as pressure distributions mainly shifted sides on the bottom surface.

Drag follows the opposite trend. It decreases in value for case 1, since now there is no high rotation to oppose the flow on the bottom surface. Additionally, a slight growth is noticeable for case 2. These changes bring an appreciable increase in L/D for case 1 and a modest decrease for case 2. Interesting to note is that L/D for case 1 is only slightly smaller than the one produced by $AdvR = 0$, which shows that applying differential rotation from case 1 to achieve better C_L is well worth the consequent increase in drag.

Rolling moment suffers an increase in magnitude in case 1 but is then drastically reduced for case 2. Pitch always seems to slightly deteriorate.

Each differential rotation case is best suited for separate goals. Case 1 is apt at increasing L/D and case 2 at minimizing the rolling moment. The latter becomes particularly useful when remembering that in a real life scenario, gyroscopic precession will occur, and added rolling moment will be induced.

7. Results for $\alpha = 10°$

7.1. Aerodynamic Coefficients

The full range of aerodynamic coefficients for a non-rotating disc ($AdvR = 0$) is summarized in Table 7.

α [°]	C_L	C_D	L/D	C_M *roll*	C_M *pitch*	C_M *yaw*
0	0	1.22 e^{-2}	0	0	0	0
5	0.181	2.56 e^{-2}	7.07	0	-4.70 e^{-2}	0
10	0.397	7.83 e^{-2}	5.07	0	-9.66 e^{-2}	0

Table 7: Mean aerodynamic coefficients for $AdvR = 0$.

These values can be compared to data from [5] and [6]. For the former, results from an elliptic wing model with $AR = 1.25$ are used for comparison. Regarding the latter, validation can be carried out by considering aerodynamic results from the thinnest disc geometry. The sign conventions from this study and [6]'s are opposite for the pitching axis. To perform validation, the obtained C_M *pitch* values from this study were made positive.

This comparison can be seen in Figures 10, 11, 12 and 13. All compared values from Table 7 agree exceptionally well with the previous studies.

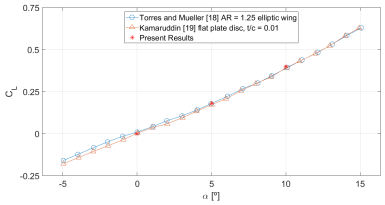

Figure 10: Comparison of obtained C_L values with previous experimental studies.

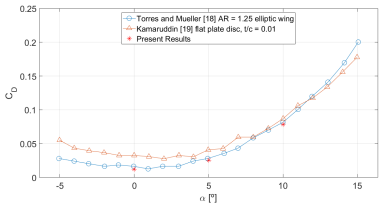

Figure 11: Comparison of obtained C_D values with previous experimental studies.

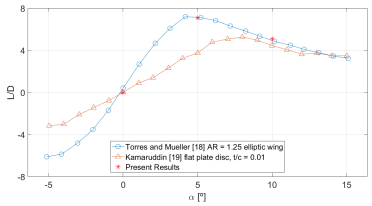

Figure 12: Comparison of obtained L/D values with previous experimental studies.

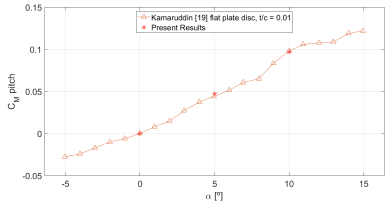

Figure 13: Comparison of obtained C_M *pitch* values with previous experimental studies.

7.2. Limiting Streamlines

Figure 14 showcases mean limiting streamlines with contours of C_p for both surfaces of the disc.

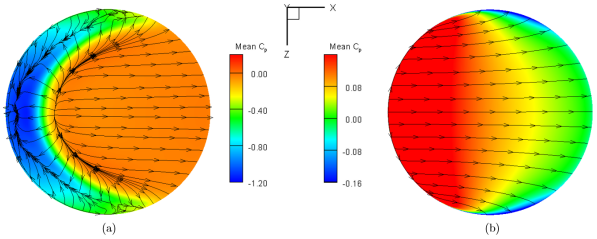

Figure 14: Mean limiting streamlines with contours of C_p for the (a) top and (b) bottom surface.

When compared to Figure 8 (a), the two separation lines representing the tip vortices now unite in one long separation, that is present near the leading edge, and an additional reattachment line is observed. This translates the appearance of a second, smaller separation bubble, encapsulated by the bigger one. Also, the original LSB increases in size, as the reattachment line signaling that the end of the bubble moves downstream. This expansion with α was noted by [9] and the resulting topology of streamlines on Figure 14 (a) is strikingly similar to the one reported on the same study, for the same angle of attack.

7.3. Differential Rotation

Differential rotation case 1 of Table 5 is applied to $\alpha = 10°$. Results are in Table 8.

Case	C_L	C_D	L/D	C_M *roll*	C_M *pitch*	C_M *yaw*
1	0.479	9.89 e^{-2}	4.84	-3.37 e^{-3}	-0.108	-5.24 e^{-2}

Table 8: Mean aerodynamic coefficients for differential rotation.

Values of C_L, C_D and C_M *pitch* all increase in magnitude, when compared to the results from Table 7. Again, L/D suffered only a slight decrease from $AdvR = 0$. The separation bubble was also fully suppressed here.

One can conclude that $AdvR = 8$ is still dominant enough to eliminate the now larger separation bubble and to generate a vast improvement in C_L over the disc without rotation, like for $\alpha = 5°$.

8. Conclusion

In conclusion, a deeper understanding of the physics governing the flight of a rotating disc at low α and at Re for typical fixed-wing MAV operation was gained. Aerodynamic data and topologies of limiting streamlines for high values of $AdvR$, otherwise missing from previous studies, were obtained.

These results will undoubtedly prove valuable for possible applications of rotating discs in MAVs, either to control flow separations, improve lift capabilities, reduce drag forces and moments as to stabilize the disc's flight, develop optimal rotation configurations for specific mission and objectives and overall contribute to the amounted knowledge of this field.

Possible future investigations are: observe the impact of changing Re on tested cases; extend the range of applied $AdvR$ to even higher values; extend the range of applied α; analyze additional combinations of differential rotation; and experimentally recreate the simulations of this study, as to ascertain their results.

Acknowledgements

A debt of gratitude is owed to my family, which always pushed me forward and helped me take the right path throughout my entire life. I would like to thank Prof. João Manuel Melo de Sousa for his undying support. His expertise, readiness to indulge in discussion and disposition to overcome any barrier in our way was what made this work possible. Last but not least, many thanks to my friends, who offered me companionship, comfort and joy during these times.

References

[1] T. J. Mueller. "Aerodynamic Measurements at Low Reynolds Numbers for Fixed Wing Micro-Air Vehicles". In *Proceedings of the Development and Operation of UAVs for Military and Civial Applications [CD-ROM], NATO RTO-EN-9*, Neuilly-sur-Seine, France, 2000.

[2] M. D. Goel and U. Rawat. "Design and Analysis of Wing Structures of Micro Air Vehicles". *Procedia Engineering*, 173:1602–1610, 2017.

[3] I. M. Al-Qadi and Ali M. Al-Bahi. "Micro Aerial Vehicles Design Challenges: State of The Art review". In *SSAS UAV Scientific Meeting and Exhibition*, Jeddah, Saudi Arabia, 2006. Paper SSAS-2006-054.

[4] G. Torres and Thomas. Mueller. "Aerodynamic Characteristics of Low Aspect Ratio Wings at Low Reynolds Numbers". In *Fixed and Flapping Wing Aerodynamics for Micro Air Vehicle Applications*, pages 115–141, 2001.

[5] G. Torres and Thomas Mueller. *"Aerodynamics of Low Aspect Ratio Wings at Low Reynolds Numbers With Applications to Micro Air Vehicle Design and Optimization"*. PhD thesis, University of Notre Dame, 2002.

[6] Noorfazreena Kamaruddin. *"Dynamics and Performance of Flying Discs"*. PhD thesis, University of Manchester, 2011.

[7] Jonathan R. Potts and William J. Crowther. "The Flow over a Rotating Disc-Wing". In *RAeS Aerodynamics Research Conference Proc.*, London, UK, Apr 2000.

[8] Jonathan R. Potts and William J. Crowther. "Frisbee^{TM} Aerodynamics". In *AIAA 2002-3150, 20th AIAA Applied Aero. Conf.*, St. Louis, MO, June 2002.

[9] H. Higuchi, Y. Goto, R. Hiramoto, and I. Meisel. "Rotating Flying Disks and Formation of Trailing Vortices". In *AIAA 2000-4001, 18th AIAA Applied Aero. Conf.*, Denver, CO, Aug 2000.

[10] Axel Rohde. *"A Computational Study of Flow Around a Rotating Disc in Flight"*. PhD thesis, Florida Institute of Technology, 2000.

[11] Stefan aus der Wiesche. "LES study of heat transfer augmentation and wake instabilities of a rotating disk in a planar stream of air". *Heat and Mass Transfer*, 40:271–284, 2004.

[12] Stefan aus der Wiesche. "Heat transfer from a rotating disk in a parallel air crossflow". *International Journal of Thermal Sciences*, 46, 2007.

[13] M. Özkan, P. J. Thomas, A. J. Cooper, and S. J. Garrett. "Comparison of the effects of surface roughness and confinement on rotor-stator cavity flow". *Engineering applications of computational fluid mechanics*, 11, 1:142–158, 2017.

[14] R. J. Lingwood. "Absolute instability of the boundary layer on a rotating disk". *Journal of Fluid Mechanics*, 299:17–33, 1995.

[15] Shintaro Imayama. *"Experimental study of the rotating-disk boundary-layer flow"*. Licentiate's thesis, KTH Royal Institute of Technology, 2012.